

# Simplified Quasi-Steady Aeromechanic Model for Flapping-Wing Robots with Passively Rotating Hinges

Zhiwei Li, Sompol Suntharasantic, and Pakpong Chirarattananon

**Abstract**—At millimeter and centimeter scales, flapping-wing robots often employ flexural passive wing hinges to eliminate extra actuation and mechanical complexity. In this paper, we propose a modified quasi-steady model for predicting aerodynamic forces from a flapping wing with a passively rotating hinge. The model is based on a simplifying assumption of balanced torque (aerodynamic torque equals to the restoring torque from the hinge). The resulting lift and drag can then be accurately predicted by the modified quasi-steady model without direct knowledge of the angle of attack of the wing. Approximate expression of stroke-averaged forces are also derived. We performed flapping experiments on a centimeter-scale device and the measured lifts show good agreement with the model predictions.

## I. INTRODUCTION

In the past decades, the growing interest in flapping-wing flight has led to vast amount of research that brings us further insights into aerodynamics and flight dynamics, from both biological perspectives [1]–[3] and engineering perspectives [4]–[7]. By studying from creatures like hummingbirds and flies, which demonstrate remarkable flight ability, researchers have developed flapping-wing micro aerial vehicles (FMAVs) that mimic biological flights [5], [7]–[9]. Unlike fixed-wing vehicles, flapping-wing vehicles have potential to be highly maneuverable and more efficient at smaller scales [10]. Nevertheless, at millimeter or centimeter scales, manufacturing of a flight capable device is challenging for several reasons, namely the stringent energetic efficiency of actuators, the required fabrication precision, and the limited payload capability [5], [6], [11].

While at millimeter scales, piezoelectric actuators have been favorably employed [5], at centimeter scales, DC motors are viable options that have demonstrated successful flapping flights [7], [9], [12]. Most robotic systems incorporate elastic components to create resonance, imitating the property of a thorax found in insects for improved flight efficiency [13]. Similarly, in these robots, the wing pitch rotation is not actively controlled, but relegated to a passive mechanism to reduce the mechanical complexity and weight [5], [7], [9], [14]. Lift is, therefore, generated by the interaction between the inertial and aerodynamic forces acting on the wing, resulting in the angle of attack. Thus far, several aerodynamics studies have taken into account the dynamics of wing rotation for prediction [15], [16],

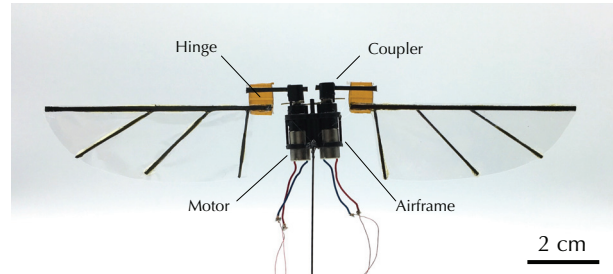


Fig. 1. Photo of a flapping-wing robot similar to the DC-motor-driven flapping wing device used for this study. The robot has a wing span of 16 cm and capable of generating 39 mN lift force, sufficient to support its 3.3-gram weight.

leading to rigorous but sophisticated models that couple aerodynamics with dynamics.

This paper is motivated by a simplifying assumption of balanced torque in the recent work [17]. That is, we follow the supposition that the restoring torque induced by a flexural wing hinge from the angle of a passively pitching wing in flapping motion is always balanced out by the torqued from aerodynamic forces (effectively neglecting the inertial term). The instantaneous angle of attack can then be determined by the speed of the wing. As a results, lift and drag coefficients for the quasi-steady model become functions of the wing speed instead of the angle of attack. This allows us to re-assess the quasi-steady model for lift and drag prediction of a flapping wing. Subsequently, without direct measurements of the angle of attack, averaged lift can be predicted from physical parameters of the wing, flapping frequency and amplitude only.

In the next section, we review the balanced torque assumption, followed by a derivation of the modified quasi-steady model for lift and drag prediction. We also offer an approximate explicit solutions that facilitate the calculation of stroke-averaged forces. The predictions of lift force are experimentally verified on a a single-wing flapper similar to the centimeter-scale flapping-wing robot prototype in Fig. 1 with further detail described in section III. The comparison of the results are given in section IV, followed by the discussion.

## II. MODIFIED QUASI-STeady MODEL FOR FORCE PREDICTION

### A. Flapping Kinematics and Quasi-Steady Model

Here we consider a flapping system with kinematics as depicted in Fig. 2a. The wing-attached frame has the origin

<sup>†</sup>The authors are with the Department of Mechanical and Biomedical Engineering, City University of Hong Kong, Hong Kong SAR, China (email: zhiweili6-c@my.cityu.edu.hk, pakpong.c@cityu.edu.hk).

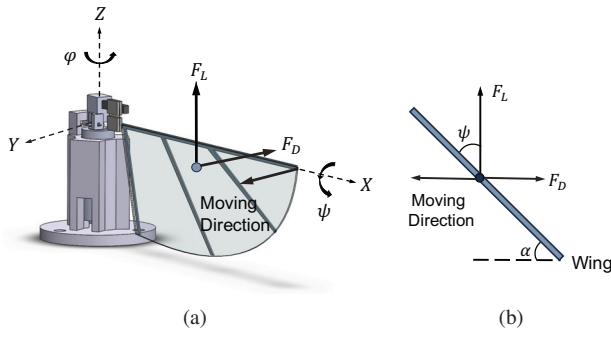


Fig. 2. Diagram of wing kinematics and forces. (a) shows the coordinate system and angles used to specify wing kinematics. (b) shows a wing during flapping, viewing from the wing tip to wing root.  $\alpha$  is the angle of attack and  $\psi$  is the wing pitch angle such that it's vertically opposite to  $\alpha$ , i.e.  $\psi = \frac{\pi}{2} - \alpha$ .

at the intersection of the wing root and the motor shaft. The leading edge coincides with the  $X$  axis and the wing is actuated to rotate about the  $Z$  axis with stroke angle  $\phi$  without an out-of-plane deviation. Lift is generated when the wing rotates about the  $X$  axis via a passive mechanism, causing the angle of attack ( $\alpha$ ) to deviate from its neutral angle of  $90^\circ$ . We define the wing hinge rotation angle ( $\psi$ ) according to Fig. 2b as the rotation of the wing about the  $X$  axis from its neutral position such that  $\psi = \frac{\pi}{2} - \alpha$ .

The morphology of the flat wing in Fig. 2a can be systematically described with the drawing in Fig. 3. We let  $r$  be the distance along  $X$  from the origin, the variable  $c(r)$  describes the chord length at position  $r$ . The total wing length is  $R$  (from the flapping axis to the wing tip). It follows that in the flapping motion when the angular stroke velocity is given by  $\dot{\phi}$ , the local velocity of the point on the wing is  $r\dot{\phi}$ . The lift ( $F_L$ ) and drag ( $F_D$ ) can be estimated by the quasi-steady model [3]

$$\begin{aligned} F_{L,D}(\psi, \dot{\phi}) &= \frac{1}{2} \rho C_{L,D}(\psi) \dot{\phi}^2 \int_{r=0}^{R_w} \int_{c'=0}^{c(r)} r^2 dc' dr \\ &= \frac{1}{2} \rho A' C_{L,D}(\psi) \dot{\phi}^2 R^2 \bar{r}_2^2 = \frac{1}{2} \rho A C_{L,D}(\psi) \dot{\phi}^2 R^2, \end{aligned} \quad (1)$$

where  $\rho$  is the air density,  $\bar{r}_2^2$  is a dimensionless  $2^{nd}$  moment of wing area [1],  $A' = R\bar{c}$  is the wing area when  $\bar{c}$  represents the mean cord, and  $A = A' \bar{r}_2^2$ , describing the effective wing area. The lift and drag coefficients can be written as functions of the wing's rotation angle [2]:

$$C_L(\psi) = C_{L0} \sin(2\psi) \quad (2)$$

$$C_D(\psi) = C_{D0} + C_{D1} \cos(2\psi). \quad (3)$$

The numerical coefficients ( $C_{L0} = 1.8, C_{D0} = 1.9, C_{D1} = 1.5$ ) were empirically determined and used for other flapping wings at similar scales [2], [15], [18].

### B. Passive Wing Pitch Rotation

In [17], the authors proposed an assumption to simplify the analysis of a flapping wing with passive pitch rotation. To elaborate, a passively pitching wing is allowed to rotate

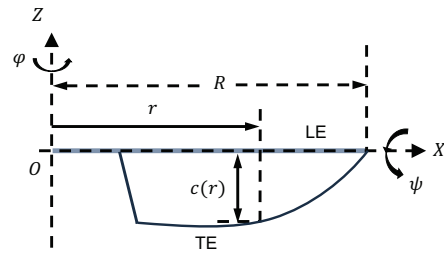


Fig. 3. Parameters of wing shape:  $R$  is the wing length,  $O$  is wing root,  $c(r)$  is the chord length at distance  $r$  from  $O$ , which is the distance between the leading edge (LE) and the trailing edge (TE),  $\phi$  is the stroke angle or the flapping angle,  $\psi$  is the passive rotation angle.

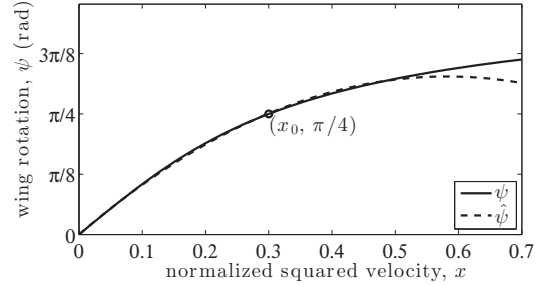


Fig. 4. The predicted wing rotation according to the normalized squared velocity according to Eq. 6. Also shown is the approximate polynomial function ( $\hat{\psi}(x)$ ) as given in Eq. 4.

about the  $X$  axis in Fig 2, 3 thanks to the incorporation of a flexural hinge. The rotation produces a restoring torque approximately proportional to the rotational stiffness of the hinge ( $k$ ). This restoring torque ( $-k\psi$ ) is assumed balanced by the torque induced by aerodynamic forces. The total aerodynamic torque about the  $X$  axis ( $\tau_{aero}$ ) can be calculated as the sum of lift and drag elements acting normal to the wing according to Fig. 2b and Eq. (1) as:

$$\tau_{aero} = \frac{1}{2} \rho (C_L \sin \psi + C_D \cos \psi) \dot{\phi}^2 \int_{r=0}^R \int_{c'=0}^{c(r)} cr^2 dc dr. \quad (4)$$

By defining

$$\begin{aligned} F &= F_L \sin \psi + F_D \cos \psi \quad \text{and} \\ r_{cp} &= \frac{\int_{r=0}^R \int_{c'=0}^{c(r)} c' r^2 dc' dr}{\int_{r=0}^R \int_{c'=0}^{c(r)} r^2 dc' dr}, \end{aligned} \quad (5)$$

we get  $\tau_{aero} = r_{cp} F$  and the assumption of balanced torque becomes  $k\psi = F r_{cp}$ . The quantity  $r_{cp}$  is often referred to as the centre of pressure [17]. Substituting the expression of  $F_{L,D}$  from Eq. (1) and of  $F$  from Eq. (5) into  $k\psi = F r_{cp}$  yields

$$\frac{1}{2k} \rho A R^2 r_{cp} \dot{\phi}^2 = \frac{\psi}{\sin(\psi) C_L(\psi) + \cos(\psi) C_D(\psi)}. \quad (6)$$

This equation suggests that, given the values of  $C_{L0}, C_{D0}, C_{D1}$ , the wing rotation angle solely depends on the dimensionless quantity on the left hand side. This dimensionless quantity consists of morphological wing parameters,

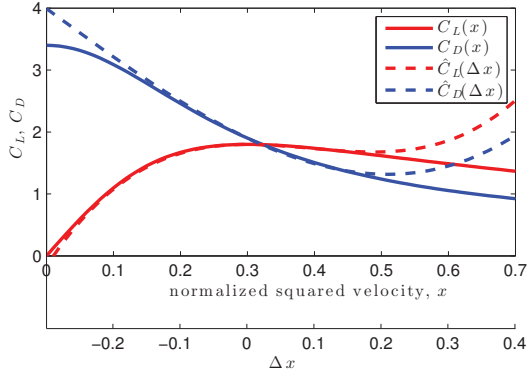


Fig. 5. Lift and drag coefficients as a function of normalized squared velocity from the model the approximate model in the polynomial form.

the hinge stiffness, and the rotational rate. That is, we let  $x$  denote the normalized squared stroke velocity such that  $x = \frac{1}{2k} \rho A R^2 r_{cp} \dot{\phi}^2$ , then  $x = f(\psi)$ , and the instantaneous wing rotation  $\psi$  can be numerically determined by using  $\psi = f^{-1}(x)$ . Fig. 4 illustrates how  $\psi$  varies as the normalized squared velocity increases. Note that since  $x$  represents a dimensionless quantity, this figure is relevant to all flapping wing systems with similar lift and drag coefficients. With the knowledge of  $\psi$ , one can proceed to determine  $C_L(\psi)$  and  $C_D(\psi)$  (and hence  $F_L$  and  $F_D$ ) without direct measurements of  $\psi$ . However, there exist a slight complication as there exists no closed-form solution of the equation  $\psi = f^{-1}(x)$ . Herein, we propose that, as long as  $x < 0.54$  or  $\psi < \pi/3$  (in other words, the wing does not rotate significantly further than  $\pi/4$ , where the maximum lift is achieved), then the approximation

$$\hat{\psi}(x) = a_1 x + a_2 x^2, \quad (7)$$

where  $a_1 = 3.54$  and  $a_2 = -3.04$  is highly accurate with the maximum error  $|\psi - \hat{\psi}|$  of 0.02 rad as shown in Fig. 4.

### C. Approximate Lift and Drag

In robotics applications, oftentimes researchers employ quasi-steady models to predict stroke-averaged lift and drag forces. In this section, we aim to obtain approximate analytical expressions of  $F_L$  and  $F_D$ . Using the introduced notation,  $x$ , it turns out that we may re-write Eq. (1) as

$$F_{L,D} = \frac{k}{r_{cp}} x C_{L,D}(x),$$

where we have used  $\psi = f^{-1}(x)$  to directly treat  $C_{L,D}$  as functions of  $x$ . Fig. 5 demonstrates how  $C_L$  and  $C_D$  changes as the stroke velocity or  $x$  increases. With the proposed approximation of  $f^{-1}(x)$  given by Eq. (7), it is possible to estimate  $F_{L,D}$  as

$$\begin{aligned} F_L &\approx \frac{k}{r_{cp}} x C_{L0} \sin [2(a_1 x + a_2 x^2)] \\ F_D &\approx \frac{k}{r_{cp}} x \{C_{D0} + C_{LD1} \cos [2(a_1 x + a_2 x^2)]\} \end{aligned} \quad (8)$$

In a number of robotic flapping devices, an elastic component is incorporated into the actuator-transmission-wing system to produce an efficient flapping mechanism capable of resonance. In such cases, the wing trajectory is approximately sinusoidal, e.g.,  $\phi(t) = \phi_0 \sin \omega t$  (where  $\phi_0$  is a flapping amplitude and  $\omega$  is the angular flapping frequency). The corresponding  $x(t)$  takes the form of  $x(t) \sim \omega^2 \phi_0^2 \cos^2 \omega t$ . When this is substituted into Eq. (8), the expression becomes increasingly sophisticated for the calculation of average forces. While it is possible to numerically evaluate the stroke-averaged lift and drag, we also propose to estimate Eq (8) further using Taylor-series expansion.

It can be seen that  $C_L$  and  $C_D$  may be expanded on the assumption of  $x \rightarrow 0$ . However, the resultant estimates will be inaccurate as  $x$  can often be as large as or larger than  $\sim 0.3$  to when  $\psi \sim \pi/4$  to  $\pi/3$ . Alternatively, we opt to expand  $C_L$  and  $C_D$  about  $x_0$ , defined such that  $\psi(x_0) = \psi/4$ . Correspondingly, we get  $x_0 = 0.30$  and  $x = x_0 + \Delta x$ . This leads to

$$\begin{aligned} \hat{C}_L(\Delta x) &= C_{L0} [1 - 2(a_1 + 2a_2 x_0)^2 \Delta x^2 \\ &\quad - 4a_2(a_1 + 2a_2 x_0) \Delta x^3] \\ \hat{C}_D(\Delta x) &= C_{D0} + C_{D1} [-2(a_1 + 2a_2 x_0) \Delta x - 2a_2 \Delta x^2 \\ &\quad + \frac{4}{3}(a_1 + 2a_2 x_0)^3 \Delta x^3], \end{aligned} \quad (9)$$

where the estimates of  $C_L$  and  $C_D$  are accurate up to  $\mathcal{O}(\Delta x^3)$ . Fig. 5 confirms that  $\hat{C}_L$  and  $\hat{C}_D$  only slightly deviate from the exact values when  $|\Delta x| < 0.2$ . For a flapping-wing robot designed to avoid over-rotation, it is expected that  $\Delta x < 0.2$  (corresponding to  $\psi < \pi/3$ ). It follows that we can estimate lift and drag forces as

$$\begin{aligned} \hat{F}_{L,D}(\Delta x) &= \frac{k}{r_{cp}} x \hat{C}_{L,D} \\ \hat{F}_L(\Delta x) &= \frac{k}{r_{cp}} C_{L0} [x_0 + \Delta x - 2x_0(a_1 + 2a_2 x_0)^2 \Delta x^2 \\ &\quad - (2a_1^2 + 12a_1 a_2 x_0 + 16a_2^2 x_0^2) \Delta x^3 \\ &\quad - 4a_2(a_1 + 2a_2 x_0) \langle \Delta x^4 \rangle] \\ \hat{F}_D(\Delta x) &= \frac{k}{r_{cp}} \{C_{D0}(x_0 + \Delta x) \\ &\quad + C_{D1} [-2x_0(a_1 + 2a_2 x_0) \Delta x \\ &\quad - 2(a_1 + 3a_2 x_0) \Delta x^2 \\ &\quad + \left(\frac{4}{3}(a_1 + 2a_2 x_0)^3 x_0 - 2a_2\right) \Delta x^3 \\ &\quad + \frac{4}{3}(a_1 + 2a_2 x_0)^3 \Delta x^4\} \}. \end{aligned} \quad (10)$$

It turns out that the relatively large errors introduced when  $\Delta x < -0.2$  or when  $x \approx 0$  do not play an important role to the resultant estimates of  $F_{L,D}$  as  $\hat{F}_{L,D} = \frac{k}{r_{cp}} x \hat{C}_{L,D} \rightarrow 0$  as  $x \rightarrow 0$ . This is confirmed by the plot of estimated lift and drag compared to their true values in Fig. 6. For a flapping wing with a simple sinusoidal wing trajectory  $\phi(t) = \phi_0 \sin \omega t$  mentioned earlier, we can define  $x_m = \frac{1}{2k} \rho A R^2 r_{cp} \omega^2 \phi_0^2$  such that  $x(t) = x_m \cos^2 \omega t$  and  $\Delta x(t) =$

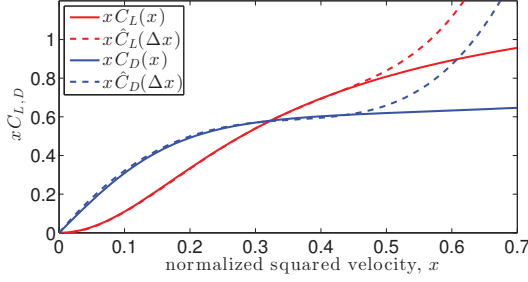


Fig. 6. Normalized lift and drag forces against  $x$  as calculated from the true model and approximate model. The approximate model is accurate when  $x < 0.5$ , corresponding to the wing rotation  $\phi < \pi/3$ .

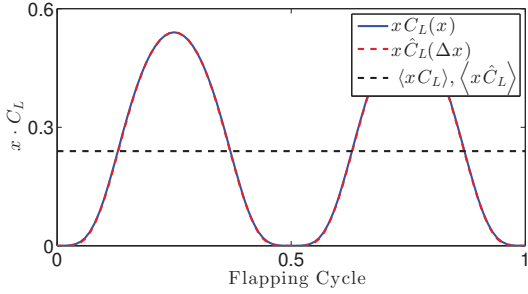


Fig. 7. The predictions of normalized lift force over one flapping cycle from the high fidelity model and the approximate model. Both models agree well. The predicted averaged lifts are also within 1% of each other.

$x_m \cos^2 \omega t - x_0$ . It is then straightforward to obtain the stroke-averaged estimates of lift and drag ( $\langle F_{L,D} \rangle$ ) from Eq. (10) by substituting in the averages of  $(\Delta x)^i$ , which can be found as follows:

$$\begin{aligned} \langle \Delta x \rangle &= \frac{x_m}{2} - x_0, & \langle \Delta x^2 \rangle &= \frac{3}{8}x_m^2 - x_mx_0 + x_0^2, \\ \langle \Delta x^3 \rangle &= \frac{5}{16}x_m^3 - \frac{9}{8}x_m^2x_0 + \frac{3}{2}x_mx_0^2 - x_0^3, \\ \langle \Delta x^4 \rangle &= \frac{35}{128}x_m^4 - \frac{5}{4}x_m^3x_0 + \frac{9}{4}x_m^2x_0^2 \\ &\quad - 2x_mx_0^3 + x_0^4. \end{aligned} \quad (11)$$

It is important to note that the expression of  $F_D$  we use does not take into account the direction of the force, it is, therefore, only valid over half a flapping cycle. The stroke-averaged drag should, in fact, be zero. To illustrate the accuracy of estimated lift for a sinusoidal wing trajectory, we provide a plot of instantaneous lift and time-averaged lift over one flapping cycle for a hypothetical trajectory that has the maximum wing rotation angle of  $\pi/4$  in Fig. 7 in the unit of normalized force ( $xC_L$ ). This figure shows that the estimate matches the true value almost perfectly. The stroke-averaged normalized lifts of the estimate and the true value are 0.2404 and 0.2396. This suggests that, with only the knowledge of wing morphology, flapping frequency, and amplitude (without measurements of instantaneous or maximum wing rotation angle), the proposed approximate expressions of lift and drag have potential to accurately predict the instantaneous and time-averaged aerodynamic forces produced by a flapping-wing robot.

### III. DESIGN, FABRICATION AND CHARACTERIZATION OF THE ROBOT

#### A. Flapping-Wing Device

The robot half is directly driven by a DC motor. The system consists of a torsional spring, a hinge and a wing. The spring confines the rotational movement of the wing to the mechanical ground, acting as an elastic element to create the resonance similar to the system described in [7]. The motor BO-P1B with stall torque of 1.765 N·mm was selected to drive the robot half. In addition to the rotation of the motor shaft that induces the flapping angle  $\phi$ , the wing also rotates passively along its leading-edge direction with the angle  $\psi$  via a flexural hinge.

The wing is made from carbon fiber spars, attached with a thin membrane layer (Mylar,  $6\mu\text{m}$ ). An assemble jig is used for the alignment of the carbon fiber rods to ensure consistent results. The wing used on the flapping-wing robot has an area of  $1165 \text{ mm}^2$  with the total length  $R = 72.1 \text{ mm}$ . The  $r_{cp}$  of the wing is 15.9 mm. The second moment of wing radius  $\hat{r}_2^2$  is 0.344. The effective wing area  $A$ , which is the product of actual wing area and the  $\hat{r}_2^2$ , is  $401 \text{ mm}^2$ .

The coupler connecting the wing and the motor shaft is 3D printed from resin (Black Resin, Formlabs Form 2).

#### B. Flexural Hinge Characterization

The passively rotating hinge is manufactured following the design in [15]. The hinge is made from five layers of materials by sandwiching a flexible material between rigid structures. The top and bottom layers are 3D printed resin plates with thickness of  $500 \mu\text{m}$ , symmetrically aligned, with a gap. The middle layer is a flexural material (Kapton, Dupont, 500HN). Two pressure sensitive adhesive layers (EL-92892, Adhesives Research) are used to bond the flexural material and the resin plates. When a torque applied, it results in a bending along the middle portion of the flexure.

Rotational stiffness of the hinge can be approximated by that of a linear elastic beam deforming under an external moment as  $k = \frac{Et^3w}{12l}$ , where  $E$  represents the Young's Modulus of the flexural material with thickness  $t$ ,  $w$  and  $l$  represent the width and the length of the hinge gap. To measure the actual stiffness, the hinge is horizontally mounted with one end freely bending down as the result of gravity. Fig. 8 shows the experiment setup. By measuring the mass  $m$  of the load below the hinge, the arm length  $L_{arm}$  to the center of load, and the rotate angle  $\gamma$  from the neutral position as depicted in Fig. 8a, the stiffness  $k$  can be calculated as  $k = \frac{mgL_{arm}}{\gamma}$ . The results are plotted in Fig. 8b, giving the measured stiffness of  $0.64 \text{ Nmm}\cdot\text{rad}^{-1}$ . The hinge used in the experiments is made from Kapton with  $E = 2.5 \text{ GPa}$ ,  $t = 127 \mu\text{m}$ ,  $w = 6.7 \text{ mm}$ , and  $l = 0.55 \text{ mm}$ , which results in a theoretical stiffness of  $5.2 \text{ Nmm}\cdot\text{rad}^{-1}$ . The large discrepancy between the measurement and the theoretical values could be due to the softening fatigue effect or the strong dependent on the thickness  $t$ , which may locally vary in the actual material.

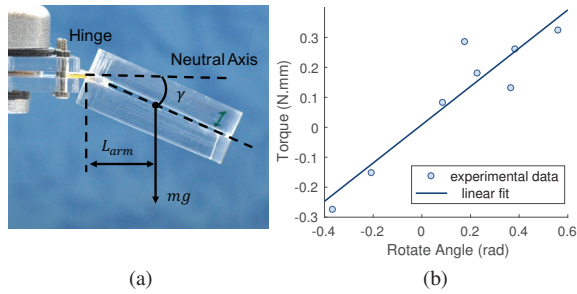


Fig. 8. Hinge stiffness test. (a) shows the experimental setup. The hinge is horizontally mounted with one end freely bending down as the result of gravity. (b) shows the results of torque plotted against the rotation angle while the slope of the fitted line indicates the hinge stiffness.

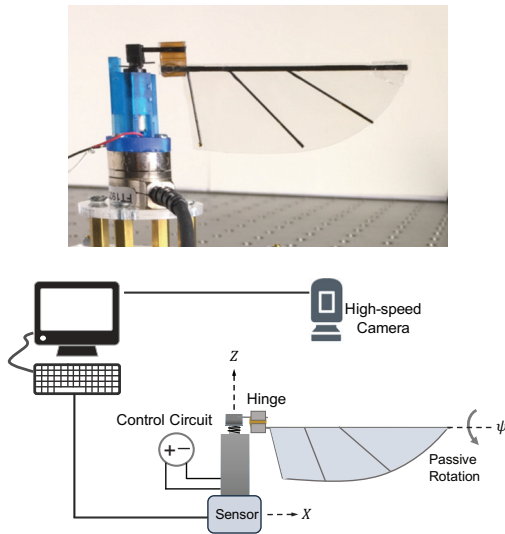


Fig. 9. Diagram of the experimental setup.

#### IV. FLAPPING EXPERIMENTS

##### A. Experimental Setup

1) *Setup and Data Acquisition:* A diagram of the experiment setup and data collection is presented in Fig. 9. The flapping experiments were carried out with a motor-driven robot half. The robot half was mounted directly on the multi-axis force/torque sensor (Nano17, ATI) with the wing along the sensor's  $X$  axis and flaps in the  $XY$  plane, perpendicular to the  $Z$  axis. A high-speed camera sits above the wing to capture the flapping stroke kinematics.

2) *Lift and Stroke Measurement:* The lift force measured by the sensor corresponds to force along the  $Z$  axis of the sensor. According to the data sheet, the sensor's resolution for force measurement along its  $Z$  axis is 3.125 mN (318 mgf). However, our calibration tests showed that the sensor is sensitive to the operating condition, and its resolution is affected by the change of temperature. Thermally insulating the sensor dramatically improves the resolution. We performed a calibration experiment with proof masses with varying weights from  $\sim 1$  to 20 mN and the results in Fig. 10 suggest that the resultant resolution of the sensor is far superior to the number provided in the data sheet. For 10 force

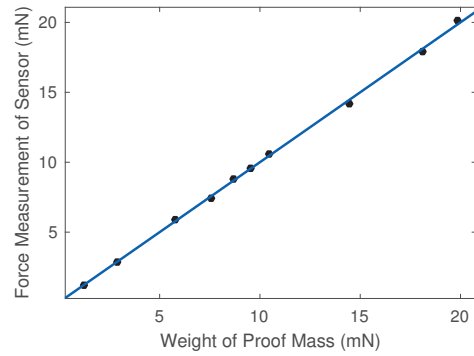


Fig. 10. Sensor resolution verification data. The measured force is plotted against the weight of proof masses.

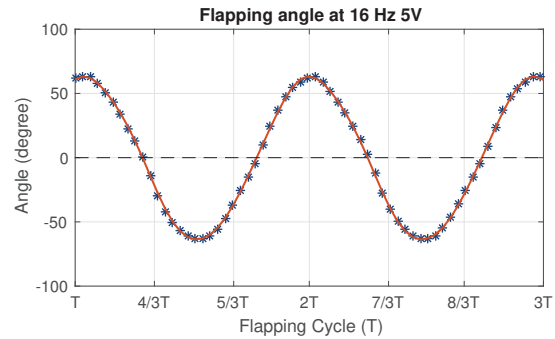


Fig. 11. Flapping stroke of the robot operating at 16 Hz with 5 V sinusoidal input.

measurements (from a digital scale with 0.1 mg precision), the RMS error is 0.16 mN (16 mg). This proves that the lift measurements from the sensor would be sufficiently accurate for a flapping wing system with the averaged lift force in the order of 10 mN.

The wing's flapping kinematics is obtained from the video captured by the high-speed camera at 1440 fps for two flapping cycles. The video is evenly divided to extract 60 frames for manual tracking of wing tip position. The stroke angle data are then fitted with a sinusoidal function with the same frequency as the driving signals. Fig. 11 shows an example of the stroke data obtained and the corresponding sinusoidal fit with the sinusoidal input voltage of 5 V at 16 Hz. The amplitude of the fitted function is treated as a flapping amplitude.

##### B. Flapping Experiments and Results

The experiments were conducted by driving the DC motor with sinusoidal inputs ranging from 3 V to 5 V, at different frequencies in the range of 13 Hz to 19 Hz with an increment of 0.5 Hz. The force and torque data along the  $X$ ,  $Y$  and  $Z$  axis of the sensor were collected and recorded using the xPC system (Mathworks) at 5 kHz, together with the current and voltage data of the motor. The average lifts are taken from the average of 30-50 flapping cycles. This results in the total of 23 data points.

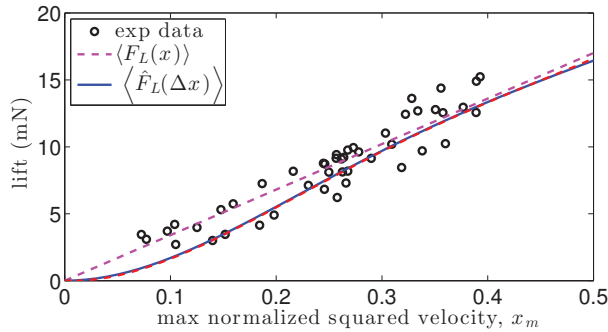


Fig. 12. The experimental lift measurements plotted against the maximum normalized squared velocity ( $x_m$ ). The model predictions are also shown in solid lines, with a linear fit that corresponds to an assumption of a constant  $C_L$ .

Fig. 12 shows the main experimental result. Here, the time-averaged lift is plotted against the maximum normalized stroke velocity ( $x_m$ ) defined in section II-C. The values of  $x_m$  are calculated from the wing morphological parameters, the flapping frequency, and the measured stroke amplitude. The lift predictions from the direct calculation ( $\langle F_L \rangle$ ) and the approximation ( $\langle \hat{F}_L \rangle$ ) based on the proposed models are also shown. The experiment was carried out over a range of  $x_m$ , from  $\sim 0.1$  to  $\sim 0.4$ .

It can be seen that, the experimental data are generally in agreement with the models. The deviations from the predictions are not more significant than the variation between trials with similar  $x_m$ . According to the model, the maximum wing rotation did not exceed  $\pi/3$  in any trial.

In addition to the proposed model, we also observe that, for  $x_m$  in this range, the relationship between  $x_m$  and lift is also approximately linear. The linear relationship would be consistent with the assumption that in all trials, the wing maintained a constant rotation angle (and hence, resulting in a constant lift coefficient,  $C_L$ ). The best fit linear line in Fig. 12. corresponds to a constant  $C_L$  of 1.7. The corresponding wing rotation angle is  $\sim 0.2\pi$  or  $35^\circ$ . While this linear prediction fits the results, it is difficult to predict the constant  $C_L$  of 1.7 without any prior measurements, nor does it reflect the actual flapping motion.

## V. DISCUSSION AND FUTURE WORK

In this work, we proposed to combine the quasi-steady model with the balanced torque assumption introduced in [17]. The results are the modified expression of lift and drag coefficients that are functions of the incoming air speed instead of the angle of attack or the wing rotation angle. This allows us to estimate the instantaneous lift and drag forces generated by a wing. Furthermore, we offer an approximation of aerodynamic forces in polynomial forms. This approximation facilitates the calculation of time-averaged forces for periodic flapping trajectories. We have experimentally verified that, using only the morphological wing parameters calculated from the known dimensions, the measurement of hinge stiffness, and the knowledge of flapping amplitude and frequency, we can accurately predict the mean lift force

generated by a flapping wing with a flexural hinge without direct measurements of the angle of attack.

One limitation of the current study is that we were unable to measure the angle of wing rotation to verify the prediction of some parts in the proposed model. This means that we cannot indirectly verify the value of the hinge stiffness we found in the characterization experiment. However, we also have computationally found that small changes ( $\sim 20\%$ ) in the hinge stiffness does not radically alter the predicted lift. In future, we will further investigate this phenomena experimentally.

## REFERENCES

- [1] C. Ellington, "The aerodynamics of hovering insect flight - the aerodynamics of hovering insect flight. ii. morphological parameters," *Philosophical Transactions of the Royal Society of London B: Biological Sciences*, vol. 305, no. 1122, pp. 17–40, 1984.
- [2] S. N. Fry, R. Sayaman, and M. H. Dickinson, "The aerodynamics of free-flight maneuvers in drosophila," *Science*, vol. 300, no. 5618, pp. 495–498, 2003.
- [3] D. D. Chin and D. Lentink, "Flapping wing aerodynamics: From insects to vertebrates," vol. 219, pp. 920–932, 04 2016.
- [4] J. Whitney and R. Wood, "Conceptual design of flapping-wing micro air vehicles," *Bioinspiration & biomimetics*, vol. 7, no. 3, p. 036001, 2012.
- [5] K. Y. Ma, P. Chirarattananon, S. B. Fuller, and R. J. Wood, "Controlled flight of a biologically inspired, insect-scale robot," *Science*, vol. 340, no. 6132, pp. 603–607, 2013.
- [6] P. Chirarattananon, K. Y. Ma, and R. J. Wood, "Perching with a robotic insect using adaptive tracking control and iterative learning control," *The International Journal of Robotics Research*, vol. 35, no. 10, pp. 1185–1206, 2016.
- [7] J. Zhang and X. Deng, "Resonance principle for the design of flapping wing micro air vehicles," *IEEE Transactions on Robotics*, vol. 33, no. 1, pp. 183–197, 2017.
- [8] M. Keennon, K. Klingebiel, H. Won, and A. Andriukov, "Development of the nano hummingbird: A tailless flapping wing micro air vehicle," in *AIAA aerospace sciences meeting*. AIAA Reston, VA, 2012, pp. 1–24.
- [9] L. Hines, D. Campolo, and M. Sitti, "Liftoff of a motor-driven, flapping-wing microaerial vehicle capable of resonance," *IEEE Transactions on Robotics*, vol. 30, no. 1, pp. 220–232, 2014.
- [10] U. Pesavento and Z. J. Wang, "Flapping wing flight can save aerodynamic power compared to steady flight," *Physical review letters*, vol. 103, no. 11, p. 118102, 2009.
- [11] D. Floreano and R. J. Wood, "Science, technology and the future of small autonomous drones," *Nature*, vol. 521, no. 7553, p. 460, 2015.
- [12] C. De Wagter, S. Tijmons, B. D. Remes, and G. C. de Croon, "Autonomous flight of a 20-gram flapping wing mav with a 4-gram onboard stereo vision system," in *Robotics and Automation (ICRA), 2014 IEEE International Conference on*. IEEE, 2014, pp. 4982–4987.
- [13] R. Dudley, *The biomechanics of insect flight: form, function, evolution*. Princeton University Press, 2002.
- [14] J. Zhang, F. Fei, Z. Tu, and X. Deng, "Design optimization and system integration of robotic hummingbird," in *2017 IEEE International Conference on Robotics and Automation (ICRA)*, May 2017, pp. 5422–5428.
- [15] J. Whitney and R. Wood, "Aeromechanics of passive rotation in flapping flight," *Journal of Fluid Mechanics*, vol. 660, pp. 197–220, 2010.
- [16] Y. Chen, N. Gravish, A. L. Desbiens, R. Malka, and R. J. Wood, "Experimental and computational studies of the aerodynamic performance of a flapping and passively rotating insect wing," *Journal of Fluid Mechanics*, vol. 791, pp. 1–33, 2016.
- [17] N. Gravish and R. J. Wood, "Anomalous yaw torque generation from passively pitching wings," in *2016 IEEE International Conference on Robotics and Automation (ICRA)*, May 2016, pp. 3282–3287.
- [18] J. A. Roll, B. Cheng, and X. Deng, "An electromagnetic actuator for high-frequency flapping-wing microair vehicles," *IEEE Transactions on Robotics*, vol. 31, no. 2, pp. 400–414, 2015.